

Multiferroicity in manganite/titanate superlattices determined by oxygen pressure-mediated cation defects

Li, Z.; You, Lu; Yang, Zai; Tan, H. R.; Ren, P.; Chen, Xiaofeng; Pan, J. S.; Wang, J. L.; Wang, L.; Bosman, Michel; Zhu, Weimin (EEE); Dong, Zhili

2013

Li, Z., You, L., Yang, Z., Tan, H. R., Ren, P., Chen, X. F., et al. (2013). Multiferroicity in manganite/titanate superlattices determined by oxygen pressure-mediated cation defects. *Journal of applied physics*, 113(16).

<https://hdl.handle.net/10356/99793>

<https://doi.org/10.1063/1.4802430>

© 2013 AIP Publishing LLC. This paper was published in *Journal of Applied Physics* and is made available as an electronic reprint (preprint) with permission of AIP Publishing LLC. The paper can be found at the following official DOI: [<http://dx.doi.org/10.1063/1.4802430>]. One print or electronic copy may be made for personal use only. Systematic or multiple reproduction, distribution to multiple locations via electronic or other means, duplication of any material in this paper for a fee or for commercial purposes, or modification of the content of the paper is prohibited and is subject to penalties under law.

Multiferroicity in manganite/titanate superlattices determined by oxygen pressure-mediated cation defects

Z. Li, L. You, Z. Yang, H. R. Tan, P. Ren et al.

Citation: *J. Appl. Phys.* **113**, 164302 (2013); doi: 10.1063/1.4802430

View online: <http://dx.doi.org/10.1063/1.4802430>

View Table of Contents: <http://jap.aip.org/resource/1/JAPIAU/v113/i16>

Published by the [American Institute of Physics](#).

Additional information on J. Appl. Phys.

Journal Homepage: <http://jap.aip.org/>

Journal Information: http://jap.aip.org/about/about_the_journal

Top downloads: http://jap.aip.org/features/most_downloaded

Information for Authors: <http://jap.aip.org/authors>

ADVERTISEMENT



The advertisement banner features a green and yellow background with abstract wavy lines. On the left, the text 'AIPAdvances' is displayed in a stylized font, with 'AIP' in blue and 'Advances' in green, followed by a series of orange dots. On the right, a circular seal contains the text 'Now Indexed in Thomson Reuters Databases'. Below this, a blue bar contains the text 'Explore AIP's open access journal:' followed by a list of three bullet points.

AIPAdvances

Now Indexed in
Thomson Reuters
Databases

Explore AIP's open access journal:

- Rapid publication
- Article-level metrics
- Post-publication rating and commenting

Multiferroicity in manganite/titanate superlattices determined by oxygen pressure-mediated cation defects

Z. Li,^{1,2} L. You,¹ Z. Yang,² H. R. Tan,³ P. Ren,⁴ X. F. Chen,² J. S. Pan,³ J. L. Wang,¹ L. Wang,⁴ M. Bosman,^{3,a)} W. G. Zhu,^{2,a)} and Z. L. Dong^{1,a)}

¹*School of Materials Science and Engineering, Nanyang Technological University, 50 Nanyang Avenue, Singapore 639798, Singapore*

²*School of Electrical and Electronic Engineering, Nanyang Technological University, 50 Nanyang Avenue, Singapore 639798, Singapore*

³*Institute of Materials Research and Engineering, A*STAR (Agency for Science, Technology and Research), 3 Research Link, Singapore 117602, Singapore*

⁴*School of Physical and Mathematical Sciences, Nanyang Technological University, 50 Nanyang Avenue, Singapore 639798, Singapore*

(Received 14 January 2013; accepted 18 March 2013; published online 23 April 2013)

Increasing demand for spintronic devices, such as high-density memory elements, has generated interest in magnetoelectric coupling and multiferroic materials. In heteroepitaxial structures, magnetoelectric coupling occurs only near the strained interfaces, which is why the interface-rich multiferroic multilayer/superlattice is viewed as one of the most efficient ways to enhance the magnetoelectric coupling coefficient. However, both ferroelectric and ferromagnetic properties are difficult to be maintained when materials are shrunk to ultrathin layers, forming interfacial dead layers and limiting the application of these materials in atomic-scale devices. In this work, we demonstrate that the largely suppressed multiferroic properties of the $\text{La}_{0.8}\text{Sr}_{0.2}\text{MnO}_3$ (16 unit cells)/ BaTiO_3 (12 unit cells) superlattice correlate with cation defects including both pure edge dislocations and planar defects. This conclusion is reached by combining atomic-resolution electron microscopy, piezoelectric force microscopy, and low-temperature magnetism measurements. Furthermore, it is shown that the density of the observed cation defects can be largely reduced by improving the oxygen off-stoichiometry through increasing oxygen pressure during growth, resulting in robust multiferroic properties. Only by eliminating oxygen vacancies during growth can the ferroic dead layers be further reduced. This work therefore opens the pathway for the integration of ferromagnetic and ferroelectric materials into magnetoelectric devices at diminished length scales. © 2013 AIP Publishing LLC [<http://dx.doi.org/10.1063/1.4802430>]

I. INTRODUCTION

Multiferroic materials with integrated electric and magnetic degrees of freedom serve as one of the most promising candidates for spintronics applications, such as high density storage devices.¹ Naturally occurring materials with a single multiferroic phase have limited application as their magnetoelectric couplings are often weak.² Therefore, artificial heterostructures consisting of ferroelectric and ferromagnetic materials have been engineered.¹ Interface engineering can be applied based on strain mediation,³ magnetic exchange bias,⁴ and charge-based couplings mechanisms.⁵ In the charge-based heterostructures, the valence states of the interfacial transitional metal can be manipulated by an applied electric field, resulting in tuned charge density and spin properties.^{6,7} Compared to conventional bilayer multiferroic composites, a multilayer/superlattice structure has a much higher interfacial area to volume ratio; thus, the magnetoelectric coupling effect can be greatly enhanced.^{8,9} This approach has attracted intensive research activity recently because oxide interfaces can now be defined with

atomic-scale precision following recent advances in growth technology.^{10,11}

However, as the materials are shrunk to ultrathin layers in the superlattice, the bulk ferroic properties are difficult to be maintained because of size effects.^{12,13} This problem strongly limits the magnetoelectric coupling at the nanoscale, hindering the application of multiferroic superlattices. The thickness-dependent ferroelectricity is controlled by the strength of interfacial bonding between the ferroelectric and the adjacent electrode, and by the intrinsic dipole moment at the interfaces.¹⁴ For the ferromagnetic ordering, the saturation magnetization and the ferromagnetic to paramagnetic transition temperatures are reduced by charge transfer, or by spin canting states, induced by interface reconstruction.^{15,16} Besides these intrinsic mechanisms, the physical properties are also very sensitive to extrinsic effects, such as cation non-stoichiometry—which cannot be removed by post-deposition annealing. The formation of extrinsic defects implies local fluctuations in chemical composition. Kourkoutis *et al.* revealed that the metallic ferromagnetism at room temperature can be stabilized in five-unit-cell-thick $\text{La}_{0.7}\text{Sr}_{0.3}\text{MnO}_3$ layers in the pulsed laser deposited (PLD) $\text{La}_{0.8}\text{Sr}_{0.2}\text{MnO}_3$ (LSMO)/ SrTiO_3 (STO) superlattices when the cation defects are eliminated by optimizing the laser fluence on a ceramic

^{a)}Authors to whom correspondence should be addressed. Electronic addresses: michel.bosman@gmail.com, ewzhu@ntu.edu.sg, and zldong@ntu.edu.sg

target.¹⁷ Therefore, understanding how the growth conditions mediate the cation defects and the impact on the corresponding physical properties is crucial for the performance of interface engineered superlattices at the nanoscale.

Due to the chemical stability and near-lattice match with each other, ferroelectric BaTiO₃ (BTO) and ferromagnetic LSMO can be engineered together for multiferroic superlattices.¹⁸ To utilize the conventional reflected high energy electron energy diffraction (RHEED) for *in-situ* thickness monitoring during superlattice growth, a low oxygen pressure is required to prevent significant scattering of electron beam by gas molecules in the chamber. It has also been demonstrated that BTO films grown under high oxygen pressure exhibit a more coarsened morphology, resulting in lattice strain relaxation and dislocations in the films.^{19,20} Thus, a relatively low oxygen pressure is preferred during film growth. However, as oxygen vacancies may introduce cation nonstoichiometry and structural defects during growth,²¹ possibly severely affecting the ferroelectricity, a better insight into the effect of oxygen pressure will be critical to obtain good multiferroic properties. This will be crucial for the realization of magnetoelectric coupling in superlattices structures. To explore the oxygen pressure effects, two samples were grown with different oxygen pressures, without changing other growth conditions. Oxygen nonstoichiometry was removed by annealing before the structural and properties characterizations. The microstructure analysis including the defects types and their interactions in the two samples were intensively carried out by electron microscopy at atomic resolution. Moreover, the role of these defects on the multiferroic properties, which were characterized by scanning probe microscopy techniques and temperature-dependent ferromagnetism measurements, was investigated. The subsequent discussion will treat the underlying physical mechanisms for the defects types that are mediated by oxygen pressures and the impact on the multiferroic properties.

II. EXPERIMENT

The 16 unit cells of LSMO and 12 unit cells of BTO layers were alternatively grown on TiO₂-terminated (001) STO substrates by PLD. A KrF excimer laser (COMPex 205 Fluorine from Lambda Physik) with a wavelength of 248 nm was employed with an energy density of 1.9 J/cm² and repetition of 1 Hz. The target materials were made by the conventional solid state route using stoichiometric amounts of La₂O₃, Mn₂O₃ and SrCO₃ for LSMO, and BaO and TiO₂ for BTO, respectively, as initial reagents. Powder X-ray diffraction analysis showed that the final target was single phase without any impurity peaks. The growth temperatures of LSMO and BTO were 780 and 680 °C, respectively. For sample A, the oxygen partial pressure was set to 1 Pa, these two layers were alternately deposited for 16 periods. The growth was *in situ* monitored by RHEED.²² To study the impact of cation stoichiometry and the cation defects, annealing at 780 °C for 3 h under oxygen flux was carried out twice after the deposition to exclude the effect from oxygen nonstoichiometry. Magnetic properties measurements as a function of temperature were conducted after each annealing. As there

were no differences in the magnetization vs. temperature curves, the elimination of oxygen nonstoichiometry was confirmed. The relative higher oxygen pressures during LSMO and BTO growth in the reference sample, which can be referred as sample B, were set to 16 Pa, while the other growth parameters were kept the same. After high temperature oxygen annealing, there is no change in its electrical and magnetic properties; thus, we can conclude most of the oxygen vacancies are eliminated during growth. The samples for TEM were prepared by grinding, dimpling, and ion milling in a Gatan Precision ion polishing system (PIPS). The specimens were cleaned by oxygen plasma and then transferred to the microscope for characterization. To identify the types of cation defects, both cross sectional TEM samples with zone axes of [010] and [110] were prepared. The high resolution TEM characterization was performed on JEOL 2100F microscope with a point resolution of 0.19 nm operating at 200 kV. A Philips CM300 TEM with Gatan 2000 electron energy loss spectroscopy (EELS) detector was employed for the energy filtered TEM (EF-TEM) studies. The corresponding chemical maps are acquired by selecting the EELS of Mn L_{2,3}-edge at ~640 eV and Ti L_{2,3}-edge at ~456 eV using a slit width of 5 eV. X-ray photoelectron spectroscopy (XPS) analysis of the samples was carried out by using a VG ESCALAB 220i-XL spectrometer with an Al K α monochromatic X-ray source (1486.6 eV). Its energy resolution is 0.2 eV. The piezoresponse analysis was conducted on a Cypher AFM from Asylum Research. Conductive Pt-Ir-coated silicon cantilevers were used for piezoelectric force microscopy (PFM) imaging and polarization switching studies. The local piezoresponse amplitudes during polarization switching were measured in fixed location on the thin films surface as a function of a dc switching bias. The bias was applied to the bottom electrode (the LSMO layer which is under the surface BTO) and the tip was grounded. A Quantum Design physical properties measurement system (PPMS) was used to characterize the magnetic properties. The magnetization vs. magnetic field (M-H) curve was measured at 5 K with the magnetic field applied in-plane, and the magnetization vs. temperature (M-T) curve was measured by applying a magnetic field of 1000 Oe along the in-plane direction of the films.

III. RESULTS AND DISCUSSION

A. Elemental mapping by energy filtered TEM

In order to demonstrate that the grown film has a well-defined layered structure with coherent interfaces, EF-TEM analysis was performed to disclose the elemental distribution of the chemically modulated layers. The spatial resolution of EF-TEM imaging was theoretically estimated to be better than 1 nm, by taking into account the spherical and chromatic aberrations in the image-forming lenses, as well as the delocalization of inelastic scattering of electrons. Spatial drift is also considered, as it will deteriorate the spatial resolution due to long exposure time.²³

Fig. 1 shows the conventional TEM image and the Ti and Mn chemical maps of the sample A. The thickness of each layer is estimated by the full width at half the maximum (FWHM) of the element profile peaks. It can be clearly

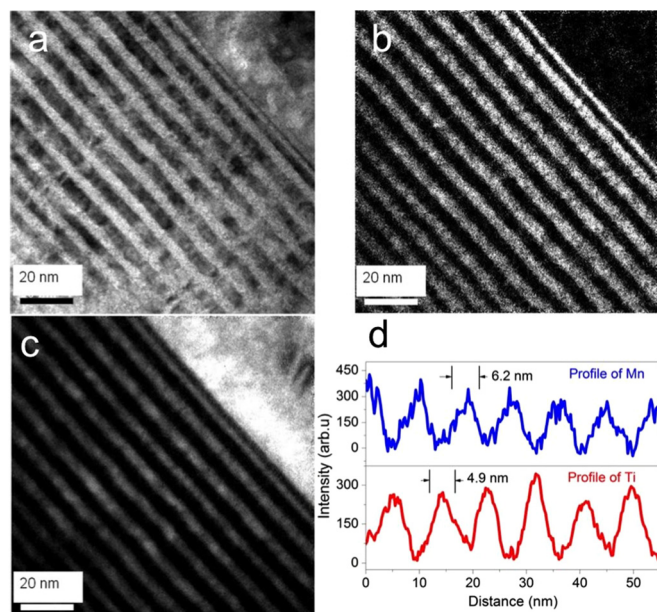


FIG. 1. (a) A corresponding conventional TEM image of sample A; the substrate is located at the top right corner. (b) Mn map and (c) Ti map by EF-TEM. The bright areas indicate the location of the mapped chemical elements. (d) EF-TEM intensity profiles of Mn (blue) and Ti (red).

observed from the Mn and Ti distributions that LSMO and BTO layers (3.2 nm each) were first successfully grown on the STO substrate, followed by periods of LSMO (6.2 nm) and BTO (4.9 nm) with stacking unit cell ratios of 4:3, as indicated in Fig. 1(d). This result approximately agrees with the estimated values from the X-ray diffraction results.²² The superlattice shows sharp, flat, and well-defined interfaces between successive LSMO and BTO layers with low concentration variation and chemical inter-diffusion below our EF-TEM resolution of about 1 nm. However, the ultrathin layers are not entirely flat, which may contribute to the mosaic structures. Below, the sample A will be studied at the atomic scale, demonstrating that defects will not only cause mosaic spread but also severely affect the ferroelectric and ferromagnetic properties.

B. Defects study by high resolution TEM

The nature of the lattice defects is studied here by atomic-resolution TEM on cross-sectional superlattice samples along the [010] and [110] zone axes. Fig. 2(a) shows the interface between substrate and film taken along the [010] direction. It presents perfect cubic-on-cubic epitaxial growth, with no amorphous layer. The selected area electron diffraction (SAED) pattern shown in Fig. 2(b) was obtained from the area covering the superlattice and partial substrate. Several weak satellite spots were clearly observed adjacent to the main diffraction spots, indicating the formation of a superlattice structure.²³ Figs. 2(c) and 2(d) are representative TEM images of sample A grown at low oxygen pressure and of sample B, respectively. The strong dependence of structural quality on the oxygen pressure is clearly visible. There are some boundary-like contrasts and blurred areas in Fig. 2(c), which is due to the strong lattice distortion or structural defects, while the contrast in Fig. 2(d) is much more uniform. The microstructure of the sample A is further studied to identify the defects types and interactions between them.

Fig. 3 shows the lattice image near the central part of sample A. Many parts of LSMO lattices are strongly distorted, as presented in Fig. 3(a). The squared areas are magnified, and the gray scale is converted into a false color representation to enhance the visibility of defects configuration.²⁴ The Burgers circuits in this study were drawn clockwise, which would be closed in a perfect crystal; the Burgers vectors were determined from the start point of the loop to the finish point.²⁵ A pure edge dislocations with Burgers vector of $a[100]$ are identified at the interface between LSMO and BTO with extra atom plane in LSMO side, and a partial defect $a/2[\bar{1}0\bar{1}]$ is found inside the LSMO layer, as shown in Figs. 3(b) and 3(c), respectively. The formation of the $a[100]$ pure edge dislocations can effectively relax the lattice mismatch strain energy, and the defect density increases as the strain increases.²⁶ Besides the $a[100]$ misfit dislocations, another type of pure edge dislocation is determined as shown in Fig. 3(d). The Burgers circuit surrounding the dislocation

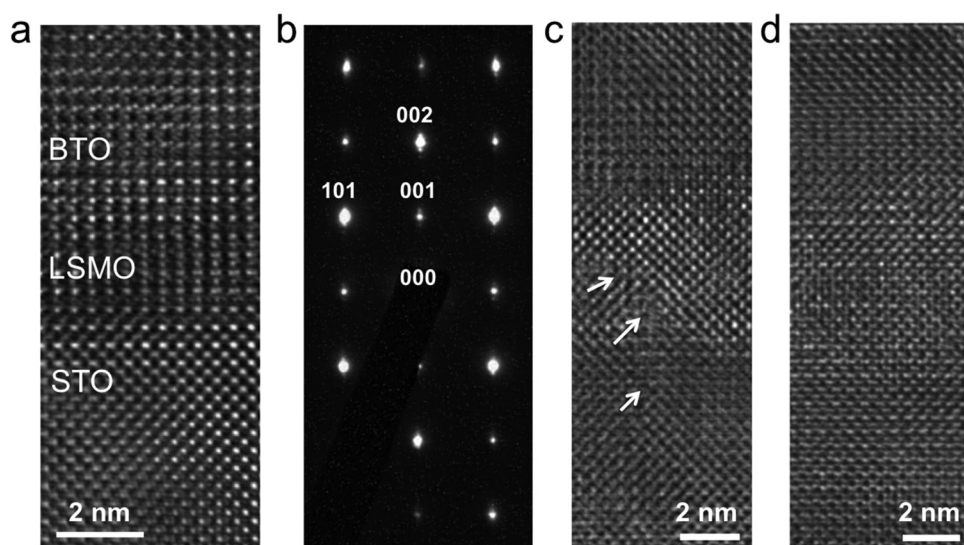


FIG. 2. (a) A HRTEM of the interface between the superlattice and the STO substrate, viewed along the [010] zone axis. (b) A SAED pattern covering whole superlattice and partially the substrate area, with the (000) diffraction spot blocked. (c) and (d) Representative HRTEM images of samples A and B (the reference), respectively. The central part is LSMO, the bottom and top layers are BTO. The arrows mark the defective area.

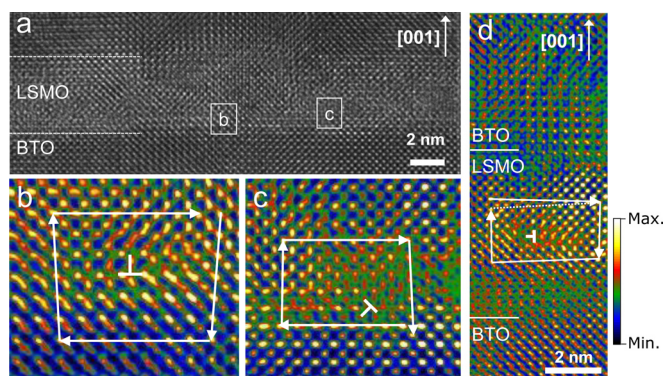


FIG. 3. (a) A high-resolution TEM image of sample A. The central area is the LSMO layer and the dashed lines indicate the interface between LSMO and BTO. The squared area b and c in (a) correspond to panels (b) and (c), respectively. (d) The another area in the LSMO.

core shows the closure vector of $a[00\bar{1}]$ along the c -axis, resulting in a lattice bending of around two degrees. This is consistent with the mosaic spread value measured by X-ray diffraction.²² In the dislocation core area, the contrast is smeared out due to the strong lattice distortion. According to the model proposed by Suzuki *et al.* and Qin *et al.*, $a(110)$ dislocation loops glide on the $\{101\}$ planes and dissociate near the interface to yield the $a[100]$ and $a[001]$ edge dislocations, where the latter are supposed to be eliminated by mutual annihilation.^{27,28} In this study, we will propose in the discussion section that the appearance of the edge dislocation with Burgers vector along c -axis was introduced by $a/2\langle 111 \rangle$ dislocations resulting from the cation nonstoichiometry.

It should be noted that, according to the Matthews-Blakeslee mechanical model, the theoretical critical thickness of BTO for a free misfit dislocation is 10 nm for a lattice misfit of 3%.²⁹ Sun *et al.* found that the critical thickness of BTO grown on STO (001) substrate is about 4 nm.²⁶ Thus, it is not arbitrary to assume that, when BTO film is only 5 nm thick, there should be very few nucleation sites for $a[100]$ defects. However, we observed distribution of $a[100]$ pure edge defects near the LSMO/BTO interface in sample A, with an average spacing of 12.4 nm as shown in Figs. 4(a) and 4(b). Therefore, to explain the observed high density of $a[100]$ interfacial edge dislocations, a mechanism will be presented in the discussion section.

Partial dislocations with Burgers vector of $a/2[\bar{1}0\bar{1}]$ as shown in Fig. 3(c) are usually accompanied by another partial dislocation, with a two-dimensional planar defect

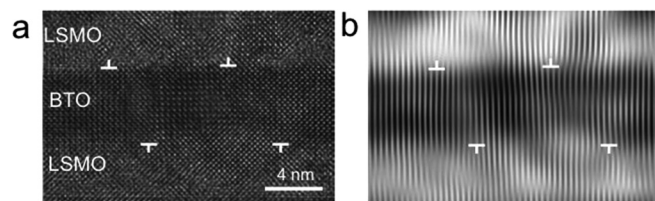


FIG. 4. (a) A high-resolution TEM image of sample A along the $[010]$ zone axis. (b) Applying (100) -Fourier filtering. The pure edge dislocations with Burgers vector of $a[100]$ near the interfaces are marked. The average spacing between them is around 12.4 nm.

sandwiched between them.²⁷ In this planar defect area, lattice distortion and composition fluctuation are then generated. As a consequence, the presence of these defects is expected to have a strong impact on the corresponding physical properties.

Two types of planar defects were observed in this study, presented separately in this section.

The first type is *Ruddlesden-Popper (RP) fault*. Previously, we demonstrated that A-site cation excess could be induced at LSMO interfaces when low oxygen pressures are used during growth.¹⁹ Such growth conditions were used here for the deposition of the ultrathin LSMO layers; the cation stoichiometry is therefore expected to occur. Fig. 5(a) shows a TEM image of sample A along the $[010]$ zone axis. At the bottom LSMO layer, a partial dislocation with a Burgers vector of $a/2[101]$ is identified. Meanwhile, a boundary-like contrast is observed starting from the dislocation and climbing along the film growth direction. This area (marked by the black square) is enlarged in Fig. 5(b) and color-coded to enhance the visibility of the contrast variation. The dashed white lines connecting the brighter dots near boundary indicate a shift in $c/2$ along the $[001]$ direction. The white lines mark the location of the boundary and show its zig-zag character, originating from the partial dislocation. By selecting appropriate multislice simulation parameters, the simulated TEM image in Fig. 5(c) and the lattice image of the boundary in LSMO side are matched. The former shows that two adjacent columns (or rows) of brighter dots indicate an extra plane of A-site cations (La or Sr); the darker dots represent the Mn B-site cations in this case. The observed boundary with the extra plane of A-site cations in the TEM image is determined to be an RP fault, which has

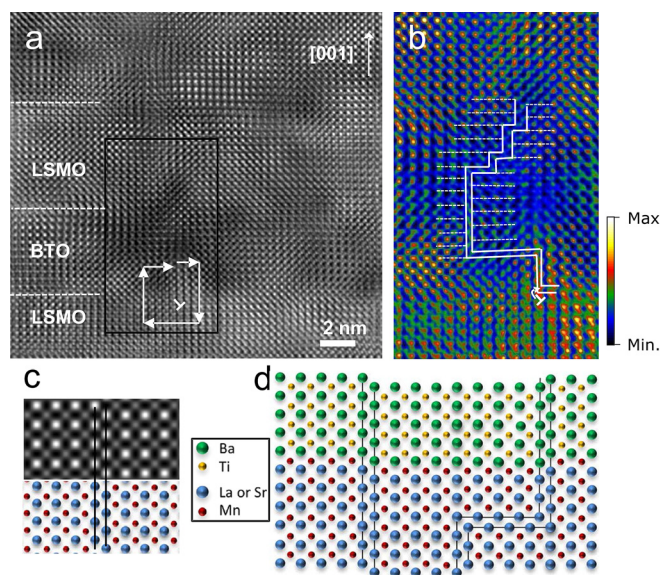


FIG. 5. (a) A high-resolution TEM image of sample A; the Burgers circuit is shown to identify the $a/2[101]$ partial dislocation. The area covered by the black square is enlarged in (b). The white lines mark the structural boundaries. The core area of the partial dislocation $a/2[101]$ is located at the turning point of the RP fault. (c) The multislice-based calculated through-focal HRTEM image of the RP fault with focus of 74 nm and thickness of 7 nm. (d) The crystallographic model for the propagation of RP faults in the LSMO/BTO heterostructure.

also been reported for Sr-rich SrTiO₃ thin films.³⁰ The existence of the RP fault is consistent with our previous finding,²¹ suggesting that this is the structural accommodation of the observed cation nonstoichiometry. The crystallographic model of the RP fault is described in Fig. 5(d). When the RP fault propagates to the surface of the LSMO layer, both (La,Sr)O and MnO₂-terminated surfaces are created. The resulting lattice displacement vector along the c-axis, therefore the RP faults, will continue in the subsequently grown BTO layer, generating possible Ba cation excess relative to Ti cations. Furthermore, the RP fault can dissociate into other types of partial dislocations, which will then produce stacking faults between them.³¹

The second type of planar defects is the *stacking fault*. Figs. 6(a) and 6(b) show a TEM image taken along the [010] zone axis, and the corresponding inverse Fourier transform image using the selected reflections (101), ($\bar{1}01$), (01 $\bar{1}$), and ($\bar{1}0\bar{1}$). The partial dislocations with a Burgers vector of $a/2[101]$ and $a/2[\bar{1}01]$ are identified according to the glide of {101} planes. It is clearly observed that the partial dislocations originate from the interface area in the LSMO and then propagate into the BTO layer, resulting in a stacking fault, which passes through the interface. The two parallel $a/2[\bar{1}01]$ partial dislocations are the dissociation of the $a[101]$ edge dislocations as indicated in the following dissociation reaction equation:²⁷

$$a[\bar{1}01] = a/2[\bar{1}01] + a/2[\bar{1}01]. \quad (1)$$

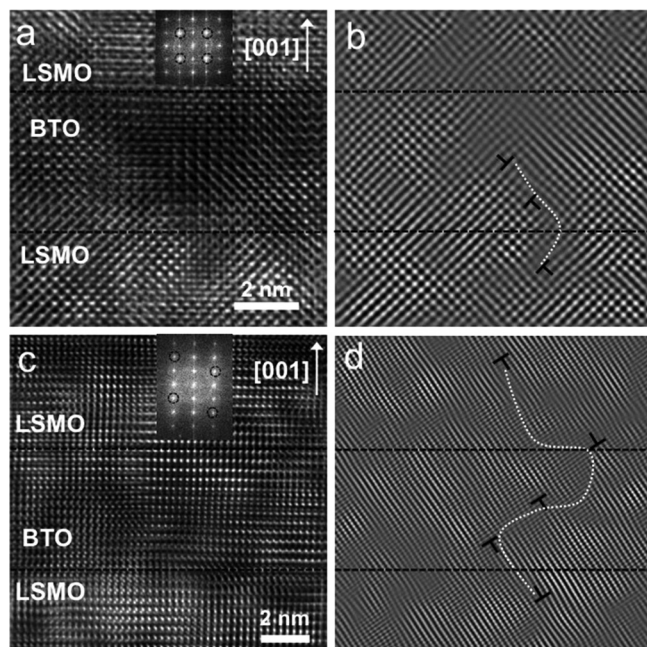


FIG. 6. (a) A high-resolution TEM image of LSMO and BTO layers viewed along the [010] zone axis in sample A. The Fourier transform of the lattice image is given in the inset. (b) The inverse Fourier transform image using the superstructure reflections indicated by the black circle in the inset of (a). The partial dislocations are marked. The trace of stacking fault is shown by the dashed white line. (c) A HRTEM image along zone axis [110]; the inset is the Fourier transform of the lattice image. (d) The inverse Fourier transform image using the superstructure reflections indicated by the black circle in the inset of (c). The dashed white line shows the trace of the connected stacking faults.

According to the Frank's rule, this dissociation reaction is energetically favorable since the $|b|^2/a^2$ value decreases from 2 to 1. Although the $\langle 110 \rangle \{ \bar{1}\bar{1}0 \}$ system is regarded as the most favorable glide system in perovskite materials,³² stacking faults in another glide system are also observed. Figs. 6(c) and 6(d) show the TEM image along the [110] zone axis and the corresponding inverse Fourier transform from the selected reflections ($\bar{1}\bar{1}2$), ($\bar{1}\bar{1}\bar{2}$), ($\bar{1}\bar{1}1$), and ($\bar{1}\bar{1}\bar{1}$). Several Frank partial dislocations with a Burgers vector of $a/3[\bar{1}\bar{1}1]$ are identified by the glide of ($\bar{1}\bar{1}2$) planes in Fig. 6(d). The stacking fault sandwiched between them is indicated by the dotted white line. The Frank partial dislocation starts from the LSMO layer, then extends into the BTO and stops in the adjacent LSMO layer. Pairs of partial dislocations connected by stacking faults can interact with each other to generate a defect network, exemplified by the white dotted line. The source of $a/3[\bar{1}\bar{1}1]$ partial dislocations could be the dissociation of $a/2[\bar{1}\bar{1}1]$ dislocations at the end of observed RP faults.³¹ For example, the following dissociation is energetically favorable:

$$a/2[\bar{1}\bar{1}1] = a/3[\bar{1}\bar{1}1] + a/6[\bar{1}\bar{1}1] \quad (2)$$

in which the $|b|^2/a^2$ value decreases from $3/4$ to $1/3 + 1/12 = 5/12$.

C. X-ray photoelectron spectroscopy analysis

Besides introducing structural defects, oxygen vacancies that are incorporated during growth will also affect the physical properties of the deposited film. Taking BTO as an example, oxygen vacancies can generate Ti³⁺ cations, replacing the stoichiometric Ti⁴⁺ cations, which might result in the degradation of the ferroelectricity. To confirm the status of the Ti cations, we have performed XPS. Figs. 7(a) and 7(b) show the XPS Ti 2p spectra obtained from samples A and B. The Ti 2p_{3/2} peaks of both samples locate at binding energy of 458 eV, which corresponds to the existence of Ti⁴⁺ cations. A careful curve fitting shows that no shoulder peak appears around 1.3 eV lower than that of Ti⁴⁺ cation, suggesting the absence of Ti³⁺ cations.³³ We therefore attribute the ferroelectric property difference between the two samples to their variation in structural defects.

D. Local ferroelectricity measured by piezoelectric force microscopy

To investigate the ferroelectricity of the topmost BTO in the superlattice, we have adapted scanning probe microscopy to perform ferroelectric poling, PFM mapping, and local switching spectroscopic measurements. Figs. 8(a) and 8(b) show the topographic images of the samples A and B, respectively. The surface of the latter is very smooth with a roughness around 0.2 nm, while the former sample has a roughness of around 0.6 nm, with some nanoscale particles found on the surface. A $4 \times 4 \mu\text{m}^2$ square area was first poled using +3 V direct current (DC) voltage, followed by a reversal of the polarization in the central $1 \times 1 \mu\text{m}^2$ region under -3 V. After relaxing for half an hour, the polarization was read under alternating current (AC) voltage of $V_{pp} \sim 0.3$ V. The out-of-plane piezoresponse phase (OPP) contrast in sample A gradually

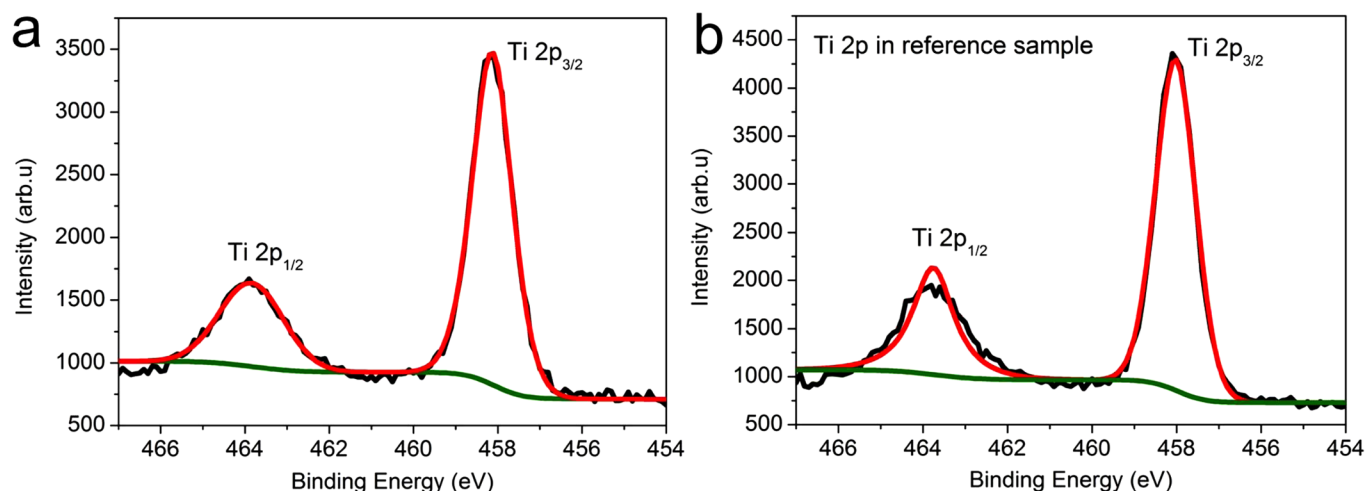


FIG. 7. XPS spectra of Ti 2p states in (a) sample A and (b) sample B (the reference sample).

faded away as shown in Fig. 8(c), suggesting weak or unstable ferroelectricity. In sample B, large OPP contrast was observed, shown in Fig. 8(d), indicating that ferroelectric domains with opposite polarizations have been successfully written on the topmost BTO layer in sample B.

Besides the phase signals, the out-of-plane ferroelectric amplitudes are measured during polarization switching. As shown in Fig. 9(a), the amplitude of the piezoresponse in sample A is near-linearly proportional to the bias voltage, indicating nearly no remnant ferroelectricity. Fig. 9(b) was measured on sample B, showing a typical ferroelectric response during the switching process. Together with the phase information, we can evidently conclude that the BTO layer in sample A has

deteriorated ferroelectricity, while BTO in sample B maintains robust ferroelectricity. In addition, conducting AFM was used to measure the current vs. voltage curves of both samples. The tunneling electroresistance (TER) effect, which originates from the ferroelectricity inside ultrathin films, was observed in sample B.³⁴ However, the TER effect was absent in sample A, indicating its weak ferroelectricity. The details can be found in the supplementary material.³⁵

E. Magnetic properties

In order to understand the interplay of the observed defects and the magnetic properties of the superlattice,

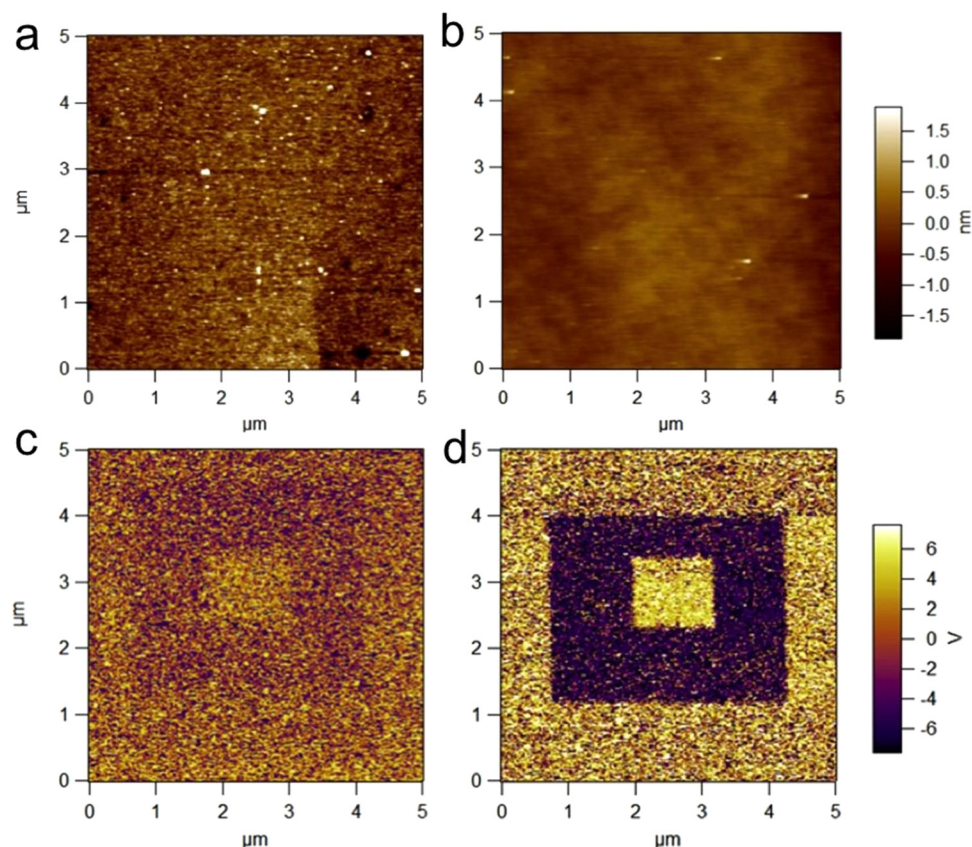


FIG. 8. (a) and (b) Topography of the superlattice samples A and B, respectively. (c) and (d) The PFM images of the polarization pattern scanned with an AFM tip on sample A and B, respectively. The purple region corresponds to polarization switched downwards (with tip bias +3 V); the yellow region in the centre corresponds to polarization switched upwards (with tip bias -3 V).

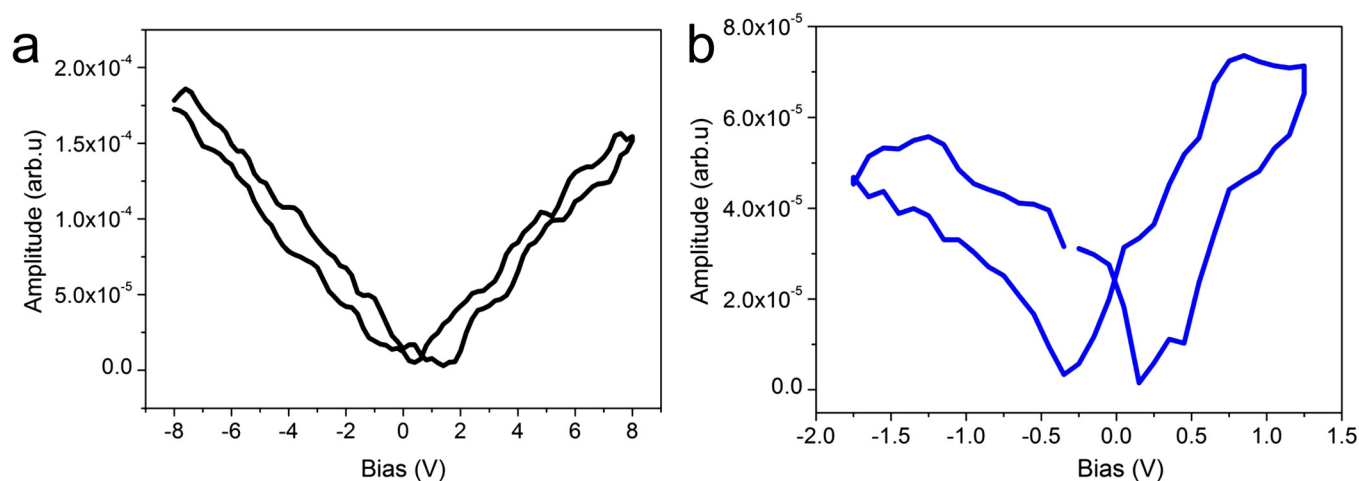


FIG. 9. The out-of-plane PFM amplitude measured on the superlattice sample A (a) and sample B (b).

magnetic measurements at low temperatures were performed. The magnetism in the superlattice arises from the LSMO layers; thus, the crystallinity and composition of LSMO dominates the measured magnetic properties. Fig. 10(a) shows the magnetic hysteresis loop of both the samples A and B, measured at 5 K. The coercivity of the sample A is 190 Oe. The saturation magnetization of the sample A is 90% lower than that of the sample B, which exhibits nearly bulk values. Fig. 10(b) shows the magnetization vs. temperature diagram. The Curie temperature of the sample A is around 260 K, while a value of 290 K is found for the sample B. Previously, we demonstrated that annealed LSMO films (80 nm thick) grown at low oxygen pressures have an almost nonferromagnetic layer near the interface, becoming more ferromagnetic closer to the free surface.²¹ Then, according to this cation nonstoichiometry dominated mechanism, the saturation magnetization value is expected to decrease as the film thickness reduces, which is clearly observed in the ultrathin LSMO layers in this study.

F. Discussion

It was found here that the oxygen pressure during film growth determines to a great extent the cation defects in the superlattices and, therefore, its multiferroic properties. These defects will still be present after post-deposition oxygen annealing, due to the very low mobility of the substitutional cations once the layers are formed. According to earlier reports, the BTO films grown under low oxygen pressure prefer layer-by-layer growth mode, achieving high crystalline quality.^{19,20} These results and our observation in this work are in conflict. Here, we propose a mechanism to solve this discord. The underlying mechanism for cation defects formation in LSMO is based on the combination of oxygen vacancies and the tensile stress from the adjacent BTO. To neutralize the positive charge induced by the oxygen vacancies, the B-site Mn cations (with oxidation states of +3 or +4) could be substituted by La and Sr cation (the oxidation states are +3 and +2, respectively). Meanwhile the A-site cation excess can increase the lattice constant of LSMO and

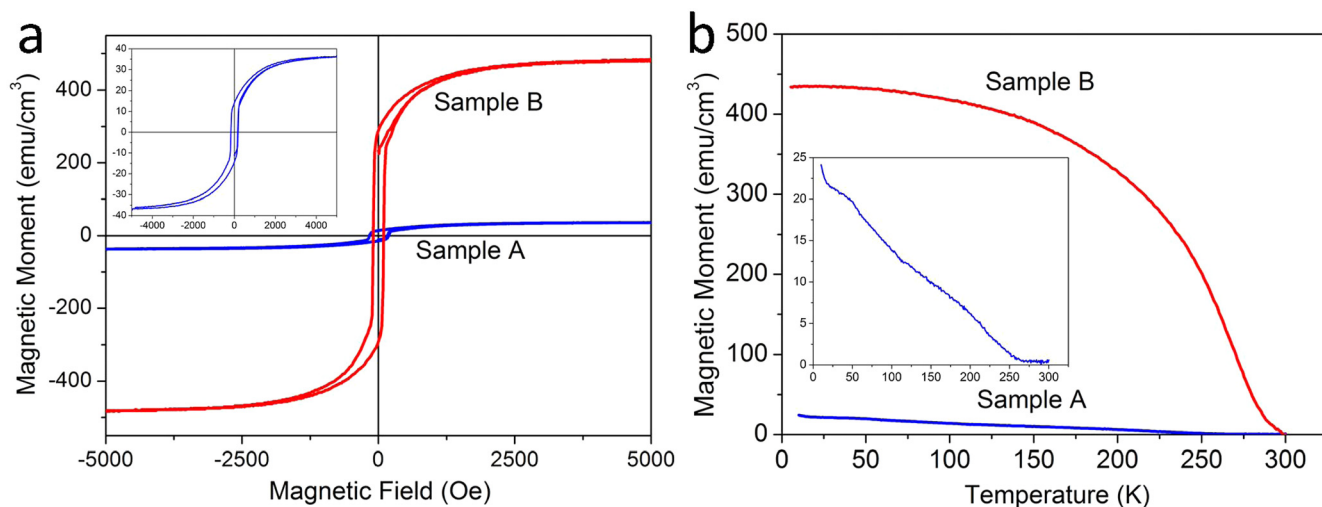


FIG. 10. Magnetic properties of LSMO in superlattices. (a) Magnetic hysteresis loop of the sample A and B at 5 K. The inserted graph is a magnification of the magnetic hysteresis loop from sample A, showing the magnetization reversal processes with small saturation magnetization. (b) Magnetization vs. temperature (M-T) curves of samples A and B. The inset is the M-T curve of the sample A; the ferromagnetic to nonferromagnetic transition temperature is 260 K.

relieve the epitaxial strain from BTO.²¹ This cation nonstoichiometry in LSMO is accommodated by the introduction of extended RP faults. As the RP faults propagate to the LSMO surface, the surface terminations at the two sides of an RP fault boundary are different, one is Mn-O₂ terminated and the other is (La,Sr)-O terminated. Subsequently, a BTO layer is deposited on this surface along the [001] direction; as the Ba-O atomic layer and Ti-O₂ atomic layer will be on the same level, indicating the RP faults propagate into the BTO, producing A-site cations (Ba) excess relative to B-site cations (Ti). The two ends of the planar defect are $a/2\langle 111 \rangle$ partial dislocations. To release the strain energy, some $a/2\langle 111 \rangle$ dislocations can dissociate into Frank partial dislocations with Burgers vectors of $a/3\langle 111 \rangle$ and $a/6\langle 111 \rangle$, producing stacking faults with a shear vector of $a/3\langle 111 \rangle$. In addition, a superdislocation, such as the $\langle 110 \rangle$, $\langle 001 \rangle$, $\langle 111 \rangle$, or null type, can be formed due to various arrangements of the extra lattice plane associated with the $a/2\langle 111 \rangle$ dislocations, while the formation of $\langle 110 \rangle$ in-plane dislocation is the most effective way to release epitaxial strain.²⁹ To explain the observed high density of $a[100]$ interfacial edge dislocations, we proposed that the RP faults induced $\langle 110 \rangle$ -type dislocations loops glide on the $\{101\}$ planes and dissociate near the interface to yield the $a[100]$ and $a[001]$ dislocations. This explanation is supported by the model proposed by Suzuki *et al.*²⁷ and Qin *et al.*²⁸ However, according to their model, the $a[001]$ dislocations are supposed to be eliminated by mutual annihilation. We proposed that the following dislocation reaction between the $a/2\langle 111 \rangle$ partial dislocations can reduce the strain energy and generate the $a[001]$ edge dislocation along c -axis direction:

$$a/2[\bar{1}\bar{1}1] + a/2[111] = a[001] \quad (3)$$

in which the $|b|^2/a^2$ value decreases from $3/4 + 3/4 = 3/2$ to 1.

As a result, the observed RP faults and $a/2\langle 111 \rangle$ dislocations accommodate the cation nonstoichiometry that was induced by low oxygen pressure during growth. Furthermore, the interactions between defects produce extra pure edge defects to release the strain energy, such as $a[100]$ and $a[001]$ edge dislocations, or stacking faults with a shear vector of $a/3\langle 111 \rangle$ within the $\langle 111 \rangle\{11\bar{2}\}$ glide system.

The suppressed ferroelectricity in the sample A is explained by using the concepts of the local strain field, cation nonstoichiometry, and charged domains induced by dislocations. Chu *et al.* visualized that the strain fields of edge type dislocations extend into PbZr_{0.2}Ti_{0.8}O₃ nanoislands and induce ferroelectric instability.³⁶ Alpay *et al.* developed a thermodynamic model based on the Landau-Devonshire formalism to study the role of dislocations in ferroelectric materials. They found that the coupling of the polarization and the strain field around the dislocations can result in a strong depolarization field that can suppresses the ferroelectricity over several nanometers.³⁷ This effect can be enhanced in ultrathin ferroelectric layers such as our BTO film since the defective area-to-volume ratio increases. By employing a negative spherical aberration imaging technique, Jia *et al.* revealed that the strain field of the $a[011]$

dislocation in the SrTiO₃ substrate can propagate across the interface into a PbZr_{0.2}Ti_{0.8}O₃ film, leading to a strong reduction of the c -axis parameters and a decrease of local spontaneous polarization.³⁸ From the reciprocal space mapping and the detection of the $a[00\bar{1}]$ and of $a[100]$ edge dislocations, the sample A was demonstrated to have mosaic structures, leading to severe lattice bending and local strain fields around dislocations. Together with the cation nonstoichiometry (possible Ba cations excess) induced by the RP fault boundaries, the atomic ordering in a large part of our BTO film deviates from the regular perovskite structure, resulting in very weak ferroelectricity. Additionally, the cation nonstoichiometric RP faults in BTO can locally induce net negative charge since the Ba²⁺ cations replace the Ti cations (with oxidation states of +3 or +4). Then, electrical fields which can couple with strain fields are built-in along the zig-zagged RP fault area. As a result, a strong depolarization field can be formed, strongly suppressing the ferroelectricity, forming ferroelectric dead layers. As the oxygen pressure increases during growth, the cation off-stoichiometry of LSMO and the RP faults can be removed due to the elimination of oxygen vacancies effect. Then the crystalline quality of subsequently grown BTO layer can be improved, resulting in well-strained lattices and ferroelectricity.

The impact of defects on the ferromagnetism of LSMO layers can also be explained by the oxygen pressure-induced interface cation nonstoichiometry.²¹ The ferromagnetic properties of LSMO are dominated by the double exchange mechanism where the Mn e_g electrons hop between Mn³⁺ and Mn⁴⁺ cations when their spins are parallel.³⁹ Therefore, the Mn³⁺/Mn⁴⁺ ratio (the Mn nominal valence) plays a crucial role in determining the magnetic properties. According to the magnetic phase diagram and our previous finding in LSMO grown with low oxygen pressure (1 Pa),²¹ the cation nonstoichiometric LSMO has high Mn nominal valence of around +3.6, with greatly reduced magnetization.⁴⁰ In this study, the observed RP faults contain extra A-site cation planes, forming a boundary with the rock-salt structure, which is consistent with the previous finding. Then, the A-site cation excess and depletion of Mn cations can generate a high Mn nominal valence state inside LSMO layers, resulting in ferromagnetic dead layers, explaining the strongly suppressed magnetization in sample A.

To measure the magnetoelectric coupling effect, the superlattices can, for example, be etched to isolated pillars at the micron or nanometer length scale, to prevent the short-circuiting of partial BTO layers and interfaces by conductive pinholes or particulates. By applying an external voltage on the surface BTO, the magnetization change can then be measured by the magneto-optical Kerr effect (MOKE) to determine the magnetoelectric coupling coefficient.

IV. CONCLUSION

LSMO (16 unit cells)/BTO (12 unit cells) superlattices were grown by pulsed laser deposition on STO (001) substrates. For samples grown at low oxygen pressure with oxygen vacancies introduced during growth, an A-site cation

excess is formed in LSMO, deteriorating the crystalline quality of the superlattice. This cation nonstoichiometry is accommodated by the introduction of Ruddlesden-Popper faults, which can propagate from LSMO to adjacent BTO layers, inducing possible Ba cation excess. Furthermore, stacking faults with a shear vector of $a/3\langle 111 \rangle$ within the $\langle 111 \rangle\{112\}$ glide system, and extra $a[001]$ and $a[100]$ pure edge dislocations can be produced due to the interaction between $a/2\langle 111 \rangle$ dislocations. Our detailed analysis demonstrates that both the ferroelectric and ferromagnetic properties are strongly suppressed due to the cation nonstoichiometry and local strain fields induced by the observed defects. Avoiding the occurrence of oxygen vacancies—by using an elevated oxygen pressure during growth—improves the cation off-stoichiometry, and results in a better crystalline quality and robust ferroelectric and ferromagnetic properties.

A mechanism was proposed to explain the role that oxygen pressure-mediated cation defects play in the formation of ferromagnetic and ferroelectric dead layers. Only after elimination of the defects by optimizing the oxygen pressures can multiferroic properties be made stronger and magnetoelectric coupling effects in LSMO/BTO superlattices be realized.

ACKNOWLEDGMENTS

Fruitful technical discussions with Weigang Chen, Zuhuang Chen, Chuanwei Huang, and Baomin Wang are gratefully acknowledged. This work was financially supported by Singapore A*STAR SERC, Grant No.: 102 101 0019.

- ¹R. Ramesh and N. A. Spaldin, *Nat. Mater.* **6**, 21 (2007).
- ²N. A. Hill, *J. Phys. Chem. B* **104**, 6694 (2000).
- ³H. Zheng, J. Wang, S. E. Lfland, Z. Ma, L. Mohaddes-Ardabili, T. Zhao, L. Salamanca-Riba, S. R. Shinde, S. B. Ogale, F. Bai, D. Viehland, T. Jia, D. G. Schlom, M. Wuttig, A. Roytburd, and R. Ramesh, *Science* **303**, 661 (2004).
- ⁴Y.-H. Chu, L. W. Martin, M. B. Holcomb, M. Gajek, S.-J. Han, Q. He, N. Balke, C.-H. Yang, D. Lee, W. Hu, Q. Zhan, P.-L. Yang, A. Fraile-Rodriguez, A. Scholl, S. X. Wang, and R. Ramesh, *Nat. Mater.* **7**, 478 (2008).
- ⁵J. D. Burton and E. Y. Tsymbal, *Phys. Rev. B* **80**, 174406 (2009).
- ⁶C. A. F. Vaz, J. Hoffman, Y. Segal, J. W. Reiner, R. D. Grober, Z. Zhang, C. H. Ahn, and F. J. Walker, *Phys. Rev. Lett.* **104**, 127202 (2010).
- ⁷H. J. A. Molegraaf, J. Hoffman, C. A. F. Vaz, S. Gariglio, D. D. Marel, C. H. Ahn, and J.-M. Triscone, *Adv. Mater.* **21**, 3470 (2009).
- ⁸C.-G. Duan, S. S. Jaswal, and E. Y. Tsymbal, *Phys. Rev. Lett.* **97**, 047201 (2006).
- ⁹H. Y. Hwang, Y. Iwasa, M. Kawasaki, B. Keimer, N. Nagaosa, and Y. Tokura, *Nat. Mater.* **11**, 103–113 (2012).
- ¹⁰C. A. F. Vaz, J. Hoffman, C. H. Ahn, and R. Ramesh, *Adv. Mater.* **22**, 2900 (2010).
- ¹¹J. Ma, J. Hu, Z. Li, and C.-W. Nan, *Adv. Mater.* **23**, 1062 (2011).
- ¹²M. Huijben, L. W. Martin, Y.-H. Chu, M. B. Holcomb, P. Yu, G. Rijnders, D. H. A. Blank, and R. Ramesh, *Phys. Rev. B* **78**, 094413 (2008).
- ¹³C. Lichtensteiger, J.-M. Triscone, J. Junquera, and P. Ghosez, *Phys. Rev. Lett.* **94**, 047603 (2005).
- ¹⁴C.-G. Duan, R. F. Sabirianov, W.-N. Mei, S. S. Jaswal, and E. Y. Tsymbal, *Nano Lett.* **6**, 483–487 (2006).
- ¹⁵H. Yamada, M. Kawasaki, Y. Ogawa, and Y. Tokura, *Appl. Phys. Lett.* **81**, 4793 (2002).
- ¹⁶M. Izumi, Y. Ogimoto, Y. Okimoto, T. Manako, P. Ahmet, K. Nakajima, T. Chikyow, M. Kawasaki, and Y. Tokura, *Phys. Rev. B* **64**, 064429 (2001).
- ¹⁷L. F. Kourkoutis, J. H. Song, H. Y. Hwang, and D. A. Muller, *Proc. Nat. Acad. Sci. U.S.A.* **107**, 11682 (2010).
- ¹⁸A.-M. Haghiri-Gosnet and J.-P. Renard, *J. Phys. D: Appl. Phys.* **36**, R127 (2003).
- ¹⁹J. Shin, S. V. Kalinin, A. Y. Borisevich, E. W. Plummer, and A. P. Baddorf, *Appl. Phys. Lett.* **91**, 202901 (2007).
- ²⁰T. Zhao, F. Chen, H. B. Lu, G. Yang, and Z. Chen, *J. Appl. Phys.* **87**, 7442 (2000).
- ²¹Z. Li, M. Bosman, Z. Yang, P. Ren, L. Wang, L. Cao, X. J. Yu, C. Ke, M. B. H. Breese, A. Rusydi, W. Zhu, Z. Dong, and Y. L. Foo, *Adv. Funct. Mater.* **22**, 4312 (2012).
- ²²Z. Yang, C. Ke, L. L. Sun, W. Zhu, L. Wang, X. F. Chen, and O. K. Tan, *Solid State Commun.* **150**, 1432 (2010).
- ²³J. Verbeeck, O. I. Lebedev, G. V. Tendeloo, and B. Mercey, *Phys. Rev. B* **66**, 184426 (2002).
- ²⁴C.-L. Jia, K. W. Urban, M. Alexe, D. Hesse, and I. Vrejoiu, *Science* **331**, 1420 (2011).
- ²⁵J. P. Hirth and J. Lothe, *Theory of Dislocations*, 2nd ed. (Wiley, New York, 1982).
- ²⁶H. P. Sun, W. Tian, X. Q. Pan, J. H. Haeni, and D. G. Schlom, *Appl. Phys. Lett.* **84**, 3298 (2004).
- ²⁷Y. L. Qin, C.-L. Jia, K. Urban, J. H. Hao, and X. X. Xi, *J. Mater. Res.* **17**, 3117 (2002).
- ²⁸T. Suzuki, Y. Nishi, and M. Fujimoto, *Philos. Mag. A* **79**, 2461 (1999).
- ²⁹J. W. Matthews and A. E. Blackleslee, *J. Cryst. Growth* **27**, 118 (1974).
- ³⁰Y. Tokuda, S. Kobayashi, T. Ohnishi, T. Mizoguchi, N. Shibata, Y. Ikumura, and T. Yamamoto, *Appl. Phys. Lett.* **99**, 173109 (2011).
- ³¹J. S. Wu, C. L. Jia, K. Urban, J. H. Hao, and X. X. Xi, *J. Cryst. Growth* **234**, 603 (2002).
- ³²P. Hirel, P. Marton, M. Mrovec, and C. Elsasser, *Acta Mater.* **58**, 6072 (2010).
- ³³M. Wegmann, L. Watson, and A. Hendry, *J. Am. Ceram. Soc.* **87**(3), 371–377 (2004).
- ³⁴E. Y. Tsymbal and H. Kohlstedt, *Science* **313**, 181 (2006).
- ³⁵See supplementary material at <http://dx.doi.org/10.1063/1.4802430> for I-V curves of the samples, showing voltage sweeps in positive and negative directions.
- ³⁶M.-W. Chu, I. Szafraniak, R. Scholz, C. Harnagea, D. Hesse, M. Alexe, and U. Gosele, *Nat. Mater.* **3**(2), 87–90 (2004).
- ³⁷S. P. Alpay, I. B. Misirliglu, V. Nagarajan, and R. Ramesh, *Appl. Phys. Lett.* **85**, 2044 (2004).
- ³⁸C.-L. Jia, S. B. Mi, K. Urban, I. Vrejoiu, M. Alexe, and D. Hesse, *Phys. Rev. Lett.* **102**, 117601 (2009).
- ³⁹C. Zener, *Phys. Rev.* **82**, 403 (1951).
- ⁴⁰Z. Fang, I. V. Solovyev, and K. Terakura, *Phys. Rev. Lett.* **84**, 3169 (2000).